Permanent Magnet Design for Torque Ripple Reduction in PM-Assisted Synchronous Reluctance Motors

Amin Nobahari[1], Abolfazl Vahedi*[1], Moein Farhadian[2], Ali Jafer Mahdi[3], and Mohammed Jamal Mohammed[4]

[1] School of Electrical Engineering, Iran University of Science and Technology, Tehran, Iran

[2] Department of Electrical and Computer Engineering, Isfahan University of Technology, Isfahan, Iran

[3] College of Information Technology Engineering, Al-Zahraa University for Women, Karbala, Iraq

[4] College of Medicine, University of Al-Ameed ,University of Al-Ameed, Karbala, Iraq.

Corresponding author: Abolfazl Vahedi, a.vahedi@iust.ac.ir, +98-21 73225619

Abstract: To ensure the smooth and reliable operation of high performance drives it is essential to diminish the parasitic effects such as pulsating torques produced by the traction motor. Inherent large torque ripple is accordingly the well-known challenge of Synchronous Reluctance Motors (SyRMs) for such a high-performance application. This paper aims to investigate the opportunity of SyRM torque profile smoothening via inserting the Permanent Magnet (PM) materials into the rotor structure. For this purpose, the Conventional PM assisted SyRM (CPMaSyRM) rotor and a recently introduced axially segmented rotor configuration, i.e. the axial integration of a PM rotor and a SyRM rotor, will be studied. It will be shown that although the torque ripple alleviation in the CPMaSyRM design via PMs parameters optimization is too restricted, the axially segmented design is significantly capable of pulsating torque compensation. The PM material utilization, power factor, and efficiency will also be evaluated for two motors. Furthermore, a computationally efficient algorithm will be proposed for the axially segmented rotor torque profile optimization, and the effect of axial field coupling will be discussed.

Key Words: Permanent magnet, Synchronous reluctance motor, Torque ripple, Optimization

1. INTRODUCTION

The application of Synchronous Reluctance Motors (SyRMs) in light weight electric vehicles has gained popularity in recent years [1-5]. One of the significant challenges with using the Synchronous Reluctance Motors (SyRMs) in high-performance drive systems is their relatively large torque ripple [6-9]. SyRMs are designed with high magnetic saliency to achieve the maximum reluctance torque, which usually leads to large pulsating torques amplitude, too. In other words, a trade-off should be performed between the mean torque and the ripple rate so that a smooth enough torque profile is obtained. Otherwise, the existing torque fluctuations produce undesirable vibration and acoustic noise [10] as well as deteriorate the mechanical powertrain apparatus, e.g. shaft, couplings, and gears [11, 12]. In this regard, several solutions have been studied mostly concerning the rotor flux barriers shaping and sizing [13-20]. However, the issue still remains that some mean torque is usually lost to smoothen the torque profile within a multi-objective design task.

The low power factor is the other challenge of the SyRMs [21], which is the case even in the SyRMs with large saliency ratios. This can be remarkably compensated by providing an additional source for the magnetizing field. For this purpose, Permanent Magnet (PM) materials are inserted into the rotor structure and the resulted scheme is called PM assisted SyRM (PMaSyRM). The PMs flux linkage also induces additional torque i.e. PM torque, that enhances the motor's torque capability. Numerous studies have dealt with proper selection of the PMs parameters, including volume [21, 22], size [23], and position [24, 25] to have the most gain for power factor and torque. Besides, recent studies have been conducted on advanced PM material selection [26, 27]. The reluctance torque requires equal D-axis and Q-axis armature currents to be maximized, while the induced PM torque is maximized when the current angle (CA) is perpendicular to the PMs field axis direction. This conflict has been addressed in [28-31] with asymmetric PMs positioning to displace the axis of the PMs field, and it was almost solved by [32, 33] via introducing a novel PMaSyRM configuration. In the new PMaSyRM, the rotor is integrated of a PM-less SyRM with reduced stack length, and a Surface PM (SPM) rotor, which are axially assembled on the shaft, with a certain angle with respect to each other. In fact, in the resulting rotor, the pole radial positions of the SyRM and SPM rotors are not equal, which leads

to an asymmetric design. It was shown in the mentioned studies that the new PMaSyRM is capable of producing more torque with equal PM material. Also, it was claimed that the PM-free SyRM can have thinner iron bridges that improve its magnetic saliency under load conditions. However, other potential capabilities or challenges of such design were not been addressed. The new motor, named SPM-SyRM in this paper hereafter, seems to be a potential candidate for high-performance applications.

This paper deals with some design aspects of the SPM-SyRM. The novel concepts that will be addressed in this research are:

(1) Introducing the specific capability of the SPM-SyRM configuration for torque ripple reduction

(2) Proposing a computationally cost-effective algorithm for its multi-objective design optimization, regarding the torque profile improvement

(3) The axial magnetic coupling caused by the retaining sleeve existence of the SPM segment will also be studied, which has not been considered before.

Additionally, a reference design of an optimized conventional PMaSyRM will be introduced to facilitate a comprehensive comparison and analysis of the SPM-SyRM characteristics. This paper introduces a high potential approach for torque ripple reduction of SyRMs toward using them in high-performance applications, however, specific limitations for the ripple rate value for a particular application should be assessed, individually.

2. SPM-SyRM Concept

Figure 1 illustrates the 3D view of an SPM-SyRM rotor in comparison with a conventional PMaSyRM (CPMaSyRM) case. The corresponding torque-CA curves (for constant current amplitude) are also presented in Fig. 2, the mathematical descriptions of which are as (1)-(3) for the CPMaSyRM and (4)-(6) for the SPM-SyRM.

In these equations $\overline{T}$ indicates the mean torque, L_d and L_q are the D-axis and Q-axis inductances of the CPMaSyRM, respectively, β stands for the CA with respect to the SyRM rotor D-axis, and P is the pole number.

$$\overline{T}_{CPMaSyRM} = \hat{T}_{SyRM} \sin 2\beta + \hat{T}_{PM1} \cos \beta \tag{1}$$

$$\hat{T}_{SyRM} = \frac{3P}{8}\left(L_d - L_q\right) I_m^2 \tag{2}$$

$$\hat{T}_{PM1} = \frac{3P}{4} \lambda_{PM1} I_m \tag{3}$$

$$\overline{T}_{SPM-SyRM} = l \times \hat{T}_{SyRM} \sin(2\beta) + \overline{T}_{SPM} \tag{4}$$

$$\overline{T}_{SPM} = \hat{T}_{SPM} \cos(\beta - \theta_{spm}^e) \tag{5}$$

$$\hat{T}_{SPM} = \frac{3P}{4} \lambda_{SPM} I_m \tag{6}$$

Fig. 1. 3D view of CPMaSyRM rotor and SPM-SyRM rotor and how the PMs are arranged in the rotors structure. Black arrows indicate the magnetization direction

Fig. 2. Torque-CA curve characteristics: (a) SyRM without PM, (b) CPMaSyRM, (c) SPM segment before and after angular displacement implementation, and (d) SPM-SyRM including SyRM and SPM segments

Also, λ_{PM1} and λ_{SPM} are the PM flux linkage amplitude respectively in CPMaSyRM and SPM-SyRM. Figure 3 shows the detailed assembling parameters of the SPM-SyRM rotor. The axial length ratio l in the SPM-SyRM indicates the reduced SyRM rotor axial length:

$$l = \frac{L_{SyRM}}{L_{Stack}} \tag{7}$$

Fig. 3. SPM-SyRM rotor assembling with shift angle between segments poles

Furthermore, the argument θ^e_{spm} in (5) is determined by the shift angle θ_{spm} that is implemented while assembling the SPM and SyRM rotor segments. θ_{spm} is the angular displacement between the SPM pole axis and the SyRM Q-axis, and it is calculated as (8) so that $\theta^e_{spm} = \pi / 4$ is obtained. As a result, both the reluctance torque component (the first term of (4)) and the PM component (the second term of (4)) reach their maximum value simultaneously at the same CA ($\beta = \pi / 4$ in SyRM rotor reference frame, see Fig. 2c).

$$\theta_{spm} = \frac{\pi P}{8} \tag{8}$$

This is the main advantage of the new configuration that utilizes the maximum possible reluctance torque and PM torque, while in the case of CPMaSyRM some PM torque (ΔT in Fig. 2b) is lost in the total torque. Accordingly, it is expected that more produced torque is achievable in SPM-SyRM. It should be remarked that a portion of the reluctance torque is removed in SPM-SyRM compared with CPMaSyRM due to the reduced SyRM axial length (SPM segment doesn't produce reluctance torque), however, the much enhanced utilization of the PMs material in the SPM segment can even improve the total torque.

3. On Pulsating Torque Reduction of SPM-SyRM

Smooth torque profile induction is usually desired for different high performance applications. The SPM segment can be designed independent of the SyRM rotor parameters. This makes a great opportunity toward improving the total torque ripple characteristics. The SPM-SyRM torque is the summation of the PM torque of the SPM segment and the reluctance torque of the SyRM segment as:

$$\begin{aligned} T_{SPM-SyRM}(t) &= l \times \overline{T}_{SyRM} + \overline{T}_{SPM} \\ &+ \sum_h l \times \tilde{T}_{SyRM,h} \cos(\omega_h t + \mu_{h0}) \\ &+ \sum_h \tilde{T}_{SPM,h} \cos(\omega_h t + \mu_{h2}) \end{aligned} \tag{9}$$

where $\tilde{T}$ and h indicates the harmonic torque amplitude and harmonic order, respectively. According to (9) the total mean torque is the sum of each rotor segment mean torque (i.e. $l \times \overline{T}_{SyRM} + \overline{T}_{SPM}$), and in the same way, the total harmonic torques are the sum of the harmonics produced by SPM and SyRM segments. Consequently, the hth torque harmonic can be eliminated if the following conditions are satisfied for the amplitude and the phase angle:

$$\tilde{T}_{SPM,h} = l \times \tilde{T}_{SyRM,h} \qquad (10)$$
$$\mu_{h2} = \mu_{h0} + \pi$$

The harmonic amplitude condition may be fulfilled through proper selection of l. While the phase angle condition depends on the torque waveform of the SPM rotor. In other words, the total harmonics can be diminished by the aid of SPM torque waveform shaping. The key point is that one should first investigate the capability of the SPM rotor for shaping its torque waveform. Also, it should be noted that the SPM torque waveform shape is independent of its axial length. For this task, a radially magnetized SPM is considered as shown in Fig. 4. This type of pole can be characterized by two parameters, i.e. PM arc and PM thickness, as can see in Fig. 4.

Fig. 4. One pole pitch of the SPM rotor. The magnetization direction is shown by white arrows

The PM thickness h_{pm} is usually determined regarding the desired air-gap flux density as well as the PM's magnetic working point [34]. Therefore it remarkably influences the PM material usage. Besides, it should be specified so that to avoid the risk of irreversible demagnetization.

To observe the effects of the PM arc α on the waveform of the produced torque, the analytical field solution is developed. Conformal mapping method is applied for analytical calculation of SPM torque. First, by applying complex logarithmic mapping, as in (11), the curved geometry of the motor in the S plane is mapped to a polygon in the Z plane; then, by applying the Schwarz-Christoffel mapping, as in (12) [35], the interior region of the polygon is mapped into a rectangle in the W plane.

$$z = \log(s) \qquad (11)$$

$$z = f(w) = A\int \prod_{k=1}^{n-1} (w - w_k)^{\frac{-\alpha_k}{\pi}} dw + C \qquad (12)$$

where A and C are integration constants and n is the number of polygon corners. $w_1, \ldots, w_n$ are the points in the canonical domain corresponding to the polygon corners and α_k represents the interior angles of the polygon. In this simple geometry, assuming infinite magnetic permeability for the core, the magnetic field generated by each conductor is explicitly given by Hague's field solution [36, 37]:

$$B_w = j\frac{I_i \mu_0}{4\,dy} \left[\coth\left(\frac{\pi}{2\,dy}(w - w_i)^* \right) + \coth\left(\frac{\pi}{2\,dy}(w - w_i)^* \right)^* \right] \qquad (13)$$

where, dy is the rectangle width; w_i represents the coordinate points on which the conductors with the current I_i are located and w represents the coordinates of the points in air gap for which the field is to be calculated.

By placing the current of the stator windings in (13), the resulting field ($B_{winding}$) is obtained. The permanent magnet magnetic field (B_{magnet}), assuming the unit relative permeability, is obtained by applying magnet equivalent currents in (13). The air gap field will be equal to the sum of the stator field and the permanent magnet field ($B_{air-gap} = B_{winding} + B_{magnet}$). Specifying the air gap field on the W plane, the air gap field on the Z plane can be calculated via (4) that establishes the relationship between the complex planes [36].

$$B_z = B_w \left(\frac{\partial w}{\partial z} \right)^* \tag{14}$$

where $(\partial w / \partial z)$ provides the derivative of w with respect to z. The radial component of the field is equal to the real part of the air gap field and the tangential component is equal to the imaginary part [36]:

$$\begin{aligned} B_r &= \mathrm{Re}\{B_{air-gap,z}\} \\ B_t &= \mathrm{Im}\{B_{air-gap,z}\} \end{aligned} \tag{15}$$

B_n and B_t are the radial and tangential magnetic field components, respectively. By determining the radial and tangential components of the air gap field, the electromagnetic torque can be calculated using the Maxwell stress tensor method:

$$T_{SPM} = \frac{P L_{SPM} R_g^2}{\mu_0} \int_0^{2\pi/P} B_r B_t \, d\theta \tag{16}$$

where $L_{SPM} = (1-l) L_{Stack}$ and R_g is the radial distance of the air gap. Fig. 5 shows the computed air-gap field produced by an SPM rotor for various PM arcs. The calculations have been performed for $h_{pm} = 3\,mm$. Accordingly, the SPM electromagnetic torque for 38.7 Amax phase current, is computed as in Fig. 6 (The SPM is assumed to have 4 poles with $L_{SPM} = 100\,mm$)

Fig. 5. Computed PM flux density in the air-gap for one pole pitch, analytical vs. FE results: (a) radial, and (b) tangential components

Fig. 6. Computed torque profile for various PM arc angles, analytical vs. FE

The slight difference in the field results in Fig. 5 leads to the differences in the calculated torques in Fig. 6. These minor errors are due to the different representations of the armature currents in each modeling method. Besides, the rotor PMs are considered by equivalent discrete currents in the conformal mapping method, while their representation in FE is continuous. The calculated fields approached FE results as the number of equivalent discrete currents increased in the conformal mapping method. According to the results of Fig. 6, one can see that the SPM torque waveform, i.e. the harmonics phase angles, can be changed by altering the α. Consequently, α should be determined so that the phase angle condition of (10) is satisfied. Furthermore, it is evident that although the analytical model and the FE model are in good overall agreement, there is some difference in the waveforms, especially in large α, where the effect of magnetic saturation grows. Since the torque ripple alleviation approach in the SPM-SyRM is based on accurate prediction of the torque profiles, it will be necessary to use FE analysis for the design task. This will be explained in the next section.

4. Design Procedure

This section aims to show the performance of the torque ripple reduction concept of SPM-SyRM in comparison with a CPMaSyRM. For this purpose, both cases will be optimally designed, following the procedure that is shown in Fig. 7.

Fig. 7. The implemented design procedure towards CPMaSyRM and SPM-SyRM optimization

According to Fig. 7, first, the SyRM rotor is designed so that maximum reluctance torque is produced through a single objective optimization. Indeed, the first step (mentioned by "PM-Less SyRM Design" in Fig. 7) is a single-objective optimization task. The calculated SyRM is the based design to be electromagnetically reinforced via PMs in two different ways, independently: (1) CPMaSyRM configuration, and (2) SPM-SyRM configuration. In other words, two separate optimization problems will be created in the second step, which is devoted to the PM-assisting task, each one is a multi-objective problem: maximizing the total mean torque and minimizing the total ripple rate. At this step the torque ripple alleviation capability via proper PM design will be assessed. Optimization of the CPMaSyRM is relatively straightforward: an intelligent search-based optimizer (OPT) determines the candidate designs for each iteration, which are evaluated via 2D-FE model. On the other side, the optimization procedure for the SPM-SyRM is different, since SPM-SyRMs may not be evaluated by 2D-FE model in the same way: an intelligent search-based optimizer (OPT1) determines the cross-section parameters of the SPM segment, then the torque waveform per axial length of each candidate design is computed by 2D-FE model. Another intelligent optimizer (OPT2) is then used to calculate the optimal axial length ratio for each design candidate using eq. (19), which will be presented in the next section.

*A. **Motor Specification***

Table I shows the rated specifications of the studied motors that are devoted to a light weight electric vehicle such as an electric scooter.

TABLE I
Studied Motor Rated Specifications

*B. **SyRM Design***

The general sizing of a SyRM, as well as its stator design can be executed similar to the conventional AC motors [38]. Table II presents the main dimensions along with the stator parameters, which will be kept unchanged throughout the study. A distributed winding layout with three slots per pole per phase is adopted in the stator.

TABLE II
Main Dimensions and Stator parameters

The critical task is to properly determine the rotor design parameters of a SyRM. Fig. 8 illustrates the geometrical parameters of the studied SyRM rotor. Analytical models have been developed for SyRMs with specific flux barrier geometries such as [39, 40]. However, due to the geometrical complexity of the typical SyRM rotors, as well as commonly significant magnetic saturation of magnetic circuit, Finite Elements (FE) model is the most useful method to accurately analyze their electromagnetic performance. First, the Taguchi method was applied to find a single design that can be an estimation of the optimal solution. Then, a smaller space adjacent to the estimated solution is considered as the new search space in which the FE model is directly used for optimization. In other words, the Taguchi method is used to reduce the size of the FE-based search space. The optimization variables are shown Fig. (8) to maximize the objective function (17).

$$ObjFCN = \hat{T}_{SyRM} \tag{17}$$

The results of the optimized SyRM parameters are presented in Table III. The calculated SyRM produces 8.79 N.m torque with 64% ripple. The relatively large torque ripple of the designed SyRM indicates the fact that the design process has been a single objective optimization toward the maximum possible reluctance torque. Although one can achieve less torque ripple rate by tuning the flux barriers parameters, especially their end parameters i.e. near the air-gap, it will be obtained at the cost of losing some mean torque by moving away from the single targeted maximum torque point. In this research, the torque ripple reduction through PM parameters modification will be investigated, instead.

Fig. 8. One pole pitch view of the studied SyRM along with the rotor design parameters

TABLE III
The calculated SyRM with maximized reluctance torque

C. *Conventional PM Assisting Scheme*

Figure 9a shows the parameters of PMs that are inserted into the SyRM flux barriers space. Three PMs per pole are designed and the thickness of each one depends on the size of the corresponding flux barrier. Thus, only the PMs width should be defined. The objective function of (18) is considered to be maximized, and the optimal solution is directly searched using FE model. Thanks to the topological features of CPMaSyRM, 2D-FE model can provide acceptable accuracy, therefore the optimization procedure is performed using 2D models so that significantly less computational burden is required.

$$ObjFCN = \frac{MeanTorque}{Ripple\ Rate} \tag{18}$$

The optimized CPMaSyRM will be considered as the reference design in this study.

Fig. 9. The PMs design parameters of (a) CPMaSyRM, and (b) SPM segment of SPM-SyRM

D. *SPM Design*

Fig. 9b shows the single parameter that will be calculated for SPM design optimization. The other parameter of SPM-SyRM that will be calculated within the optimization procedure is the axial length ratio l. The PMs are magnetized in the radial direction and their thickness is considered constant (3mm) to retain their magnetic working point regarding the PM utilization and demagnetization points of view [41].

The topological features of SPM-SyRM make it necessary to use 3D model for its electromagnetic analysis. However, this will lead to expressively massive computation costs if search-based optimization is to be intended. To resolve this issue a computationally cost-effective solution is proposed in this paper.

The torque profile of SPM-SyRM is the sum of the torque profiles of SPM and SyRM segments as:

$$T_{SPM-SyRM} = l \times T_{SyRM} + (1-l) L_{stack} \tau_{SPM} \tag{19}$$

In (19) τ_{SPM} is the torque waveform per axial length of SPM segment in [N.m/m]. If the axial field coupling between the rotor segments is ignored, T_{SyRM} can be considered as the value that was calculated in section 4.2, and τ_{SPM} can be calculated through 2D FE model, and the total torque can be obtained using (19). Consequently, the algorithm of Fig. 7 is used for the optimal calculation of the SPM segment. As can see in Fig. 7, the search task is shared between two optimizer units, OPT1 and OPT2, the former optimizes the PM parameter and hence $\tau_{SPM}(\alpha)$, and the latter optimizes the axial length ratio l. Thus, 2D-FE analysis is used only by OPT1, while OPT2 uses (19) for estimating the total torque profile. Therefore, remarkably fewer FE models will be computed that reduces the computation cost. Both OPT1 and OPT2 are intelligent search-based optimizers (e.g. evolutionary algorithms) to maximize the objective function of (18). It is worth noting that a design constraint is set regarding the PM volume to be equal or less than that of the case of the optimized CPMaSyRM.

In the previous studies of SPM-SyRM, the necessity of adopting a retaining sleeve for the SPM segment was not been addressed. However, it is usually vital to guarantee the mechanical stability of the surface mounted PM by a retaining sleeve for higher speed operation. Otherwise, the structural weakness of the SPM segment degrades the whole motor robustness, while the SyRMs are expected to be mechanically robust. From the magnetic point of view, the presence of the retaining sleeve increases the magnetic air-gap. Therefore the axial field coupling will be

intensified near the segments joint position which results in two issues: (1) the iron loss will be increased, and (2) the air-gap field pattern near the mentioned region will be deformed, which inversely affects the pulsating torque compensation performance of the segments. As a preliminary solution, a small axial gap can be adopted between the SPM and SyRM segments to increase the magnetic reluctance related to the undesirable axial field.

In this study, the magnetic air-gap of the SPM segment is increased to 0.9mm (0.5mm is considered for the retaining sleeve thickness) so that the mechanical air-gap is kept constant.

5. Results and Discussion

The optimized PM assisting parameters of CPMaSyRM and SPM-SyRM are presented in Table IV. The results are calculated considering NdFeB-N42 for the PMs and M800-50A electric steel for the stator and rotor cores. In this section, 3D FE models of the designed motors are developed to make the desired comparisons.

TABLE IV
The optimized parameters of CPMaSyRM and SPM-SyRM

Fig. 10 shows the loaded flux density contour computed via 3D-FE analysis of the SyRM and CPMaSyRM. In the finite elements simulations, the armature windings have been excited by current sources, similar to the equations (1)-(6). The torque profile of the designed CPMaSyRM in comparison with the PM-less SyRM is depicted in Fig. 11. One can see the effect of the additional PM torque, while the pulsating torques of the motor slightly change.

Fig. 10. 3D FE analysis of the optimized CPMaSyRM: loaded flux density contour

Fig. 11. Full load torque profile comparison of SyRM and CPMaSyRM

Fig. 12. 3D FE analysis of the optimized SPM-SyRM: loaded flux density contour without axial gap (left), and with axial gap (right)

The developed 3D-FE model of the designed SPM-SyRM is illustrated in Fig. 12. It can see heavy saturation located near the joint of the SPM and SyRM segments. The increased magnetic air-gap of the SPM segment related to the retaining sleeve has intensified the axial field coupling. Accordingly, not only the accuracy of the 2D-model-based design, which was discussed in the previous section, is decreased but also the iron loss challenge appears. As a simple solution, a small axial magnetic gap ($\approx 1mm$) can be adopted between the rotor segments. This can be easily implemented using a thin non-magnetic lamination at the desired location. The results are shown in Fig. 12, which demonstrates that the discussed saturation has been significantly eliminated.

The torque profile of the optimized SPM-SyRM is compared with that of CPMaSyRM in Fig. 13, in which one can visually find out that both the mean torque and the ripple rate have remarkably improved. It should be mentioned that equal PM material is used for both designs. However, as can see in Fig. 14, the amplitude of the PMs flux linkage of the SPM-SyRM is much improved compared with CPMaSyRM. The enhanced PM flux linkage (i.e. the enhanced PM utilization) along with the implemented shift angle θ_{spm} are the reasons for the mean torque enhancement. In order to better see the values of the improvements, the detailed information of Fig. 13, as well as the PM material usage comparison is presented in Table V. The results show that 14.8% more torque is achieved in SPM-SyRM compared with CPMaSyRM design using equal PM material. In other words, 14.8% enhanced torque density is possible using the SPM-SyRM concept since the total size of the motor is kept unchanged. The special point that is highlighted in this paper is the torque ripple alleviation capability in the SPM-SyRM configuration. As can see in Table V the ripple rate is reduced from 52.4% to 24.2% (almost 54% improvement) which is an outstanding achievement. In the case of the inverter controller (gating signal) failure at high-speed operations (much larger than the base speed), the large internal voltage poses overvoltage risks to the inverter system. Accordingly, compared with the CPMaSyRM, the much larger PM flux of the SPM-SyRM requires special considerations for the inverter over-voltage protection.

Table V also presents the comparison of the 2D FE-based prediction of the torque characteristics, which were used in the design optimization procedure, and the results that were obtained from 3D FE analysis. In Table V one can see some differences between the torque characteristics computed by 2D and 3D models. These show the errors of 2D modeling, since the axial field effects existing in two ends of the machine, as well as the joint position of the rotor segments of

SPM-SyRM, are ignored in 2D models, although it has been much reduced via implementing the axial gap.

To better see the results of the pulsating torque cancelation mechanism that was explained in section 3, the produced torque profile of each rotor segment and the total torque are illustrated in Fig. 15, in which the opposite changes of the torque harmonics of the rotor segments can be clearly observed.

Fig. 13. Full load torque profile comparison of CPMaSyRM and SPM-SyRM

Fig. 14. PMs flux linkage comparison of CPMaSyRM and SPM-SyRM

TABLE V
Torque characteristics and PM usage of the optimized designs SyRM, CPMaSyRM and SPM-SyRM

Fig. 15. Illustration of the SPM-SyRM total ripple reduction

Table VI presents the performance comparison of PM-less SyRM SPM-SyRM and CPMaSyRM in terms of power factor, loss, and efficiency. Fundamentally, by adding the PM material to the magnetic circuit, an additional induced voltage will appear along the d-axis. As a result, the terminal voltage's phasor will change so that to have a smaller angle with respect to the current phasor, i.e. smaller φ". The remarkably modified PMs flux linkage of the SPM-SyRM (see Fig. 14) leads to the much improved power factor compensation capability of this motor compared with the CPMaSyRM. Equal current is assumed for all cases, hence their copper loss (P_{copper}) is equal, too. The iron loss (P_{iron}) is calculated via post-process computations based on Bertotti's equation. The electromagnetic efficiency is:

$$Efficiency = \frac{\bar{T}_{total}\omega}{\bar{T}_{total}\omega + P_{copper} + P_{iron}} \tag{20}$$

$\bar{T}_{total}$ is the total mean torque and $\omega = \frac{4\pi f}{P}$. The power factor is calculated using the equation below, in which P_{in} is the input electric power, and V_{rms} and I_{rms} are the total RMS values of the line voltage and current, respectively.

$$PF = \frac{P_{in}}{\sqrt{3}V_{rms}I_{rms}} \tag{21}$$

The iron loss is increased in SPM-SyRM in comparison with CPMaSyRM that is mainly due to the larger flux density of the stator core section corresponding to the SPM segment. Nevertheless, the efficiency of SPM-SyRM is more than CPMaSyRM owing to the larger mean torque (output power). However, it should be noted that compared with the CPMaSyRM, the SPM-SyRM has limited performance at high speed operating regions from the loss point of view. Generally, the SPM rotor has higher iron loss compared with interior mounted PM rotors [42]. Besides, the surface PM eddy loss may be significantly challenging for high speeds, however, PM segmentation can effectively reduce this issue [43].

TABLE VI
Loss, efficiency, and power factor of the optimized designs

6. Conclusion

The concept of SPM-SyRM for torque capability and PMs utilization enhancement has been introduced in the literature. This study focused on an additional feature of such configuration that is the potential for torque ripple reduction, which was discussed from the theoretical point of view as well as a case study implementation. Besides, some design aspects were discussed including the electromagnetic effect of the retaining sleeve that is the remarkable axial field coupling between the rotor segments. A 2D model-based optimization algorithm was also introduced for optimal calculation of the SPM-SyRM rotor that is computationally easy to be executed. The study illustrates the

outstanding capability of the SPM-SyRM for compensating the large reluctance pulsating torques, which can turn it into a potential candidate for high performance drives where the high smooth torque is of great importance. It is worth mentioning that with a similar stator, same rotor size, and same PM material, the SPM-SyRM produces +14.8% more power, which means that the studied motor is almost 14.8% superior in terms of material cost. However, the comparison of the construction cost depends on the manufacturing technology, limited/mass production, etc.

References

[1] Bianchi N., Bolognani S., Carraro E., et al., "Electric vehicle traction based on synchronous reluctance motors," *IEEE Transactions on Industry Applications,* vol. 52, no. 6, pp. 4762-4769, 2016, **DOI:** 10.1109/TIA.2016.2599850

[2] Jurca N., Inţe R., Popa D., et al., "Electromagnetic and Mechanical Analysis of a Modular Outer Rotor Synchronous Reluctance Machine for Light Propulsion Vehicles," *IEEE Transactions on Transportation Electrification,* vol. 7, no. 4, pp. 2798-2811, 2021, **DOI:** 10.1109/TTE.2021.3067135

[3] Mishra S., Varshney A., Singh B., and Parveen H., "Driving-cycle-based modeling and control of solar-battery-fed reluctance synchronous motor drive for light electric vehicle with energy regeneration," *IEEE Transactions on Industry Applications,* vol. 58, no. 5, pp. 6666-6675, 2022, **DOI:** 10.1109/TIA.2022.3181224

[4] Nasiri-Zarandi R., Karami-Shahnani A., and Toulabi M. S., "Proposing an External Rotor In-Hub PM Assisted Synchronous Reluctance Motor for an E-Bike." *3rd International Conference on Electrical Machines and Drives (ICEMD),* 2023, **DOI:** 10.1109/ICEMD60816.2023.10429649

[5] Salehinia S., Afjei S., and Hekmati A., "Analytical method for optimal design of synchronous reluctance motor for electric scooter application," *Scientia Iranica,* vol. 29, no. 5, pp. 2537-2551, 2022, **DOI**: 10.24200/SCI.2021.56496.4748

[6] Diao X., Zhu H., Qin Y., and Hua Y.,"Torque ripple minimization for bearingless synchronous reluctance motor," IEEE Transactions on Applied Superconductivity, vol. 28, no. 3, pp. 1-5, 2018, **DOI:** 10.1109/TASC.2018.2798632

[7] Chen Q., Yan Y., Xu G., et al., "Principle of torque ripple reduction in synchronous reluctance motors with shifted asymmetrical Poles," IEEE Journal of Emerging and Selected Topics in Power Electronics, vol. 8, no. 3, pp. 2611-2622, 2019, **DOI:** 10.1109/JESTPE.2019.2909570

[8] Naeimi M., Nasiri-Zarandi R., and Abbaszadeh K., "C-and circular-shaped barriers optimization in a synchronous reluctance rotor for torque ripples minimization," Scientia Iranica, vol. 30, no. 3, pp. 1085-1096, 2023, **DOI**: 10.24200/SCI.2021.57254.5140

[9] Amiri A. H., Abdollahi S. E., and Hasanzadeh S., "Performance Comparison of Different Methods of Torque Ripple Reduction for Permanent Magnet-assisted Synchronous Reluctance Motor." *3rd International Conference on Electrical Machines and Drives (ICEMD),* 2023, **DOI:** 10.1109/ICEMD60816.2023.10429257

[10] Mishra A. K., Rajpurohit B. S., and Kumar R., "Revampment of surface permanent magnet synchronous motor design for ameliorated torque profile in e‐mobility applications," IET Electrical Systems in Transportation, vol. 11, no. 2, pp. 99-108, 2021, **DOI**: 10.1049/els2.12007

[11] Kia S. H., Henao H., and Capolino G.-A., "Torsional vibration assessment using induction machine electromagnetic torque estimation," IEEE Transactions on Industrial Electronics, vol. 57, no. 1, pp. 209-219, 2009, **DOI:** 10.1109/TIE.2009.2034181

[12] Wanjiku J., Khan M. A., Barendse P. S., and Pillay P., "Influence of slot openings and tooth profile on cogging torque in axial-flux PM machines," IEEE Transactions on Industrial Electronics, vol. 62, no. 12, pp. 7578-7589, 2015, **DOI:** 10.1109/TIE.2015.2458959

[13] Bacco G., and Bianchi N., "Choice of flux-barriers position in synchronous reluctance machines." pp. 1872-1879, **DOI:** 10.1109/ECCE.2017.8096023

[14] Bianchi N., Degano M., and Fornasiero E., "Sensitivity analysis of torque ripple reduction of synchronous reluctance and interior PM motors," IEEE Transactions on Industry Applications, vol. 51, no. 1, pp. 187-195, 2014, **DOI:** 10.1109/ECCE.2013.6646932

[15] Moghaddam R.-R., and Gyllensten F., "Novel high-performance SynRM design method: An easy approach for a complicated rotor topology," IEEE Transactions on Industrial Electronics, vol. 61, no. 9, pp. 5058-5065, 2013, **DOI:** 10.1109/TIE.2013.2271601

[16] Nobahari A., Vahedi A., and Mahmouditabar F., "Torque Profile Improvement of a Synchronous Reluctance Motor through Optimizing the Rotor Flux Barriers Ends." pp. 169-173, **DOI**: 10.1109/PSC49016.2019.9081540

[17] Alotto P., Barcaro M., Bianchi N., and Guarnieri M., "Optimization of interior PM motors with machaon rotor flux barriers," IEEE Transactions on Magnetics, vol. 47, no. 5, pp. 958-961, 2010, **DOI:** 10.1109/TMAG.2010.2073450

[18] Xu Y., Xu Z., Cao H., and Liu W., "Torque Ripple Suppression of Synchronous Reluctance Motors for Electric Vehicles Based on Rotor Improvement Design," IEEE Transactions on Transportation Electrification, 2022, **DOI:** 10.1109/TTE.2022.3231301

[19] Kumar N. S., and Srinivas S., "Flux-Barrier Based Rotor Design of Permanent Magnet Assisted Synchronous Reluctance Motor with Power Density and Torque ripple Improvement for e-Mobility." pp. 1-6, **DOI:** 10.1109/ITEC-India59098.2023.10471474

[20] Linh D. H., Dinh B. M., Khue T. K., and Quoc V. D., "Evaluation Of Flux-barriers For Synchronous Reluctance Motors," pp. 607-611, **DOI:** 10.1109/ICCAIS59597.2023.10382394

[21] Bianchi N., Fornasiero E., and Soong W., "Selection of PM flux linkage for maximum low-speed torque rating in a PM-assisted synchronous reluctance machine," IEEE Transactions on Industry Applications, vol. 51, no. 5, pp. 3600-3608, 2015, **DOI:** 10.1109/TIA.2015.2416236

[22] Barcaro M., Bianchi N., and Magnussen F., "Permanent-magnet optimization in permanent-magnet-assisted synchronous reluctance motor for a wide constant-power speed range," IEEE Transactions on Industrial Electronics, vol. 59, no. 6, pp. 2495-2502, 2011, **DOI:** 10.1109/TIE.2011.2167731

[23] Huynh T. A., Hsieh M.-F., Shih K.-J., and Kuo H.-F., "An investigation into the effect of PM arrangements on PMa-SynRM performance," IEEE Transactions on Industry Applications, vol. 54, no. 6, pp. 5856-5868, 2018, **DOI:** 10.1109/TIA.2018.2853042

[24] Liu H.-C., Kim I.-G., Oh Y. J., et al., "Design of permanent magnet-assisted synchronous reluctance motor for maximized back-EMF and torque ripple reduction," IEEE Transactions on Magnetics, vol. 53, no. 6, pp. 1-4, 2017, **DOI:** 10.1109/TMAG.2017.2663319

[25] Liu C.-T., Luo T.-Y., Shih P.-C., et al., "On the design and construction assessments of a permanent-magnet-assisted synchronous reluctance motor," IEEE Transactions on Magnetics, vol. 53, no. 11, pp. 1-4, 2017, **DOI:** 10.1109/TMAG.2017.2702185

[26] Jamnani J. G., and Jani S., "Performance Analysis of PM Assisted Synchronous Reluctance Motor for Different PM Materials for Electric Vehicular Application." pp. 1-6, 2023, **DOI:** 10.1109/IECON51785.2023.10312562

[27] Kumar P., Wilson R., Chowdhury T., and Ayman E.-R., "Multi-Objective Design Optimization and Comparison of 2-layer versus 3-layer PM-Assisted Synchronous Reluctance Machines using a Blend of Rare-Earth and Rare-Earth-Free Magnets." pp. 3930-3937, 2023, **DOI:** 10.1109/ECCE53617.2023.10362802

[28] Alsawalhi J. Y., and Sudhoff S. D., "Design optimization of asymmetric salient permanent magnet synchronous machines," IEEE Transactions on Energy Conversion, vol. 31, no. 4, pp. 1315-1324, 2016, D**OI:** 10.1109/TEC.2016.2575138

[29] Zhao W., Zhao F., Lipo T. A., and Kwon B.-I., "Optimal design of a novel V-type interior permanent magnet motor with assisted barriers for the improvement of torque characteristics," IEEE Transactions on Magnetics, vol. 50, no. 11, pp. 1-4, 2014, **DOI:** 10.1109/TMAG.2014.2330339

[30] Zhao W., Chen D., Lipo T. A., and Kwon B.-I., "Performance improvement of ferrite-assisted synchronous reluctance machines using asymmetrical rotor configurations," IEEE Transactions on magnetics, vol. 51, no. 11, pp. 1-4, 2015, **DOI:** 10.1109/INTMAG.2015.7156554

[31] Zhao W., Lipo T. A., and Kwon B.-I., "Optimal design of a novel asymmetrical rotor structure to obtain torque and efficiency improvement in surface inset PM motors," IEEE Transactions on Magnetics, vol. 51, no. 3, pp. 1-4, 2015, **DOI:** 10.1109/TMAG.2014.2362146

[32] Zhao W., Xing F., Wang X., et al., "Design and analysis of a novel PM-assisted synchronous reluctance machine with axially integrated magnets by the finite-element method," IEEE Transactions on Magnetics, vol. 53, no. 6, pp. 1-4, 2017, **DOI:** 10.1109/TMAG.2017.2662717

[33] Zhao W., Shen H., Lipo T. A., and Wang X., "A new hybrid permanent magnet synchronous reluctance machine with axially sandwiched magnets for performance improvement," IEEE Transactions on Energy Conversion, vol. 33, no. 4, 2018, **DOI:** 10.1109/TEC.2018.2876938

[34] He C., and Wu T., "Analysis and design of surface permanent magnet synchronous motor and generator," Ces transactions on electrical machines and systems, vol. 3, no. 1, pp. 94-100, 2019, **DOI:** 10.30941/CESTEMS.2019.00013.

[35] Driscoll T. A., and Trefethen L. N., Schwarz-christoffel mapping: Cambridge University Press, 2002, **DOI**: 10.1017/CBO9780511546808

[36] Boughrara K., Zarko D., Ibtiouen R., et al., "Magnetic field analysis of inset and surface-mounted permanent-magnet synchronous motors using Schwarz–Christoffel transformation," IEEE Transactions on Magnetics, vol. 45, no. 8, pp. 3166-3178, 2009, **DOI:** 10.1109/TMAG.2009.2016559

[37] Hague B., Electromagnetic Problems in Electrical Engineering: An Elementary Treatise on the Application of the Principles of Electromagnetism to the Theory of the Magnetic Field and of the Mechanical Forces in Electrical Machinery and Apparatus: H. Milford, 1929.

[38] Huang S., Luo J., Leonardi F., and Lipo T. A., "A general approach to sizing and power density equations for comparison of electrical machines," IEEE Transactions on Industry Applications, vol. 34, no. 1, pp. 92-97, 1998, **DOI:** 10.1109/28.658727

[39] Farhadian M., Moallem M., and Fahimi B., "Analytical calculation of magnetic field components in synchronous reluctance machine accounting for rotor flux barriers using combined conformal mapping and magnetic equivalent circuit methods," Journal of Magnetism and Magnetic Materials, vol. 505, pp. 166762, 2020, **DOI**: 10.1016/j.jmmm.2020.166762

[40] Mahmoud H., Bianchi N., Bacco G., and Chiodetto N., "Nonlinear analytical computation of the magnetic field in reluctance synchronous machines," IEEE Transactions on Industry Applications, vol. 53, no. 6, pp. 5373-5382, 2017, **DOI:** 10.1109/TIA.2017.2746560

[41] Mahmouditabar F., Vahedi A., and Ojaghlu P., “Investigation of demagnetization phenomenon in novel ring winding AFPM motor with modified algorithm,” Journal of Magnetism and Magnetic Materials, vol. 491, pp. 165539, 2019, **DOI**: 10.1016/j.jmmm.2019.165539

[42] Vagati A., Pellegrino G., and Guglielmi P., "Comparison between SPM and IPM motor drives for EV application." pp. 1-6, 2010, **DOI:** 10.1109/ICELMACH.2010.5607911

[43] Pellegrino G., Vagati A., Guglielmi P., and Boazzo B., “Performance comparison between surface-mounted and interior PM motor drives for electric vehicle application,” IEEE Transactions on Industrial Electronics, vol. 59, no. 2, pp. 803-811, 2011, **DOI:** 10.1109/TIE.2011.2151825

Biographies

Amin Nobahari received his B.S. and M.S. degrees in 2014 and 2017, respectively, from the Shahrood University of Technology, Shahrood, Iran, and his Ph.D. from the Iran University of Science and Technology, Tehran, Iran, in 2022. He has several years of experience working as an R&D and design engineer in the industry. His research interests are mostly focused on electrical machines, including modeling, design, optimization, and multi-physics analysis.

Abolfazl Vahedi (IEEE senior member) received his bachelor's degree from Ferdowsi University of Mashhad, Iran in 1989 and master's degree and Ph.D. degree in electrical engineering from the National Polytechnic Institute of Lorraine, France in 1992 and 1996. He is currently a professor in the electrical engineering department of Iran University of Science and Technology and head of the special machines and drives' laboratory.

His current research interests include design, modeling, optimization and fault diagnosis of electric machines and drives. Since 2023, he is the COB of the Scientific Association of Electric Machines and Drives of Iran.

Moein Farhadian received the M.Sc. and PhD degrees in electrical engineering from the Isfahan University of Technology, Iran, in 2017, and 2022, respectively. His research interests include electric machines modeling, analysis, and design optimization using advanced analytical and numerical methods with a special interest in synchronous and switched reluctance motors.

Ali Jafer Mahdi has received his B.Sc. and M.Sc. degrees in Electrical Power and Machines from the University of Technology (Iraq) in 1995 and 1997, respectively. In 2011, he earned his Ph.D. degree from the University of Liverpool (UK). Currently, Dr. Mahdi holds the position of Director of the Department of Scientific Affairs at Al-Zahraa University for Women in Iraq. Previously, he was the Head of the Department of Electrical and Electronic Engineering at the University of Karbala from 2013 to 2016. His research interests encompass diverse topics such as the Optimization and Control of Renewable Energy Systems, Power Electronics and Drives, Control of Electrosurgical Generators, and Wireless Power Transfer Systems.

Mohammed Jamal Mohammed born in 1986 in Karbala, Iraq, is a specialist in electrical engineering. He obtained his B.S. degree in Medical Instruments Techniques Engineering from AL Hussein University College and his M.Sc. degree in Electronic Medical Instrumentation from Middle Technical University, Baghdad in 2018 and 2020, respectively. Currently pursuing his Ph.D. degree at Babol Noshirvani University of Technology. Mohammad has experience of publishing various articles and active participation in specialized conferences.

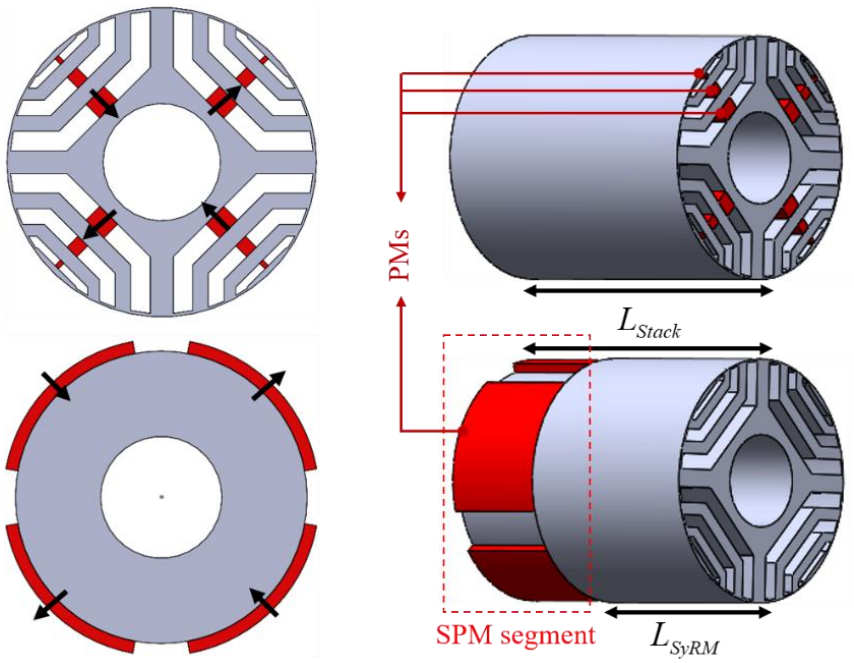

Fig. 1. 3D view of CPMaSyRM rotor and SPM-SyRM rotor and how the PMs are arranged in the rotors structure. Black arrows indicate the magnetization direction

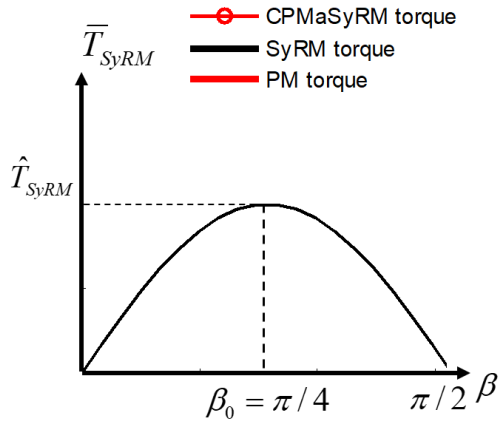

(a)

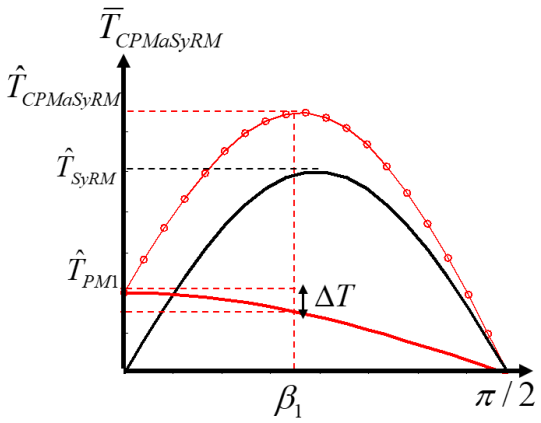

(b)

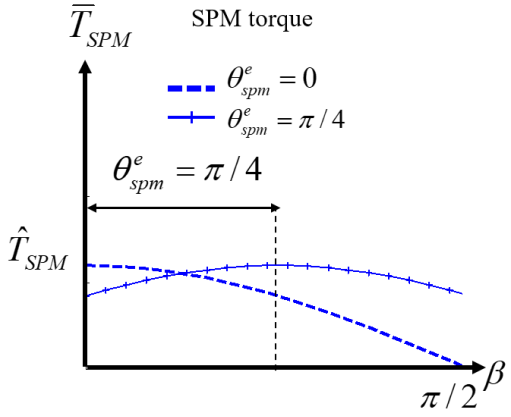

(c)

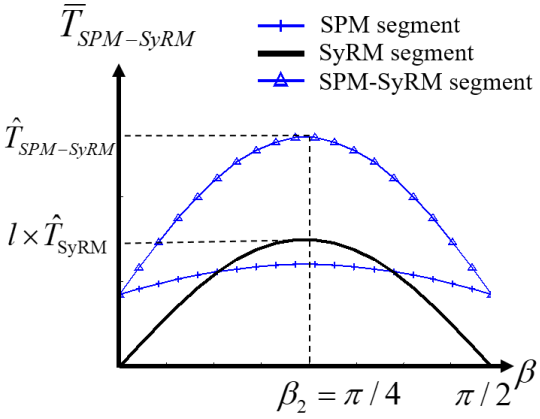

(d)

Fig. 2. Torque-CA curve characteristics: (a) SyRM without PM, (b) CPMaSyRM, (c) SPM segment before and after angular displacement implementation, and (d) SPM-SyRM including SyRM and SPM segments

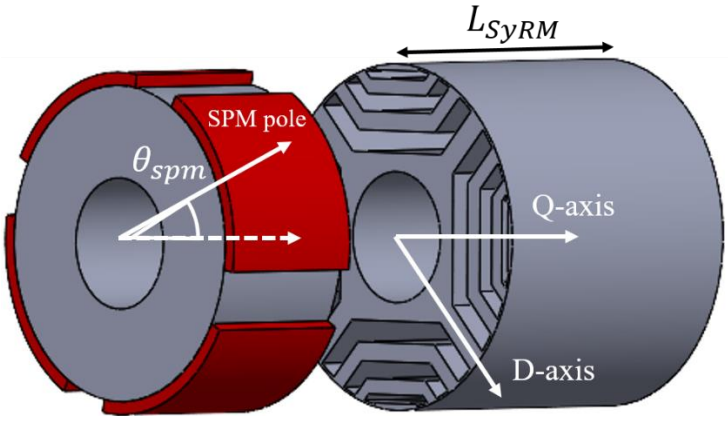

Fig. 3. SPM-SyRM rotor assembling with shift angle between segments poles

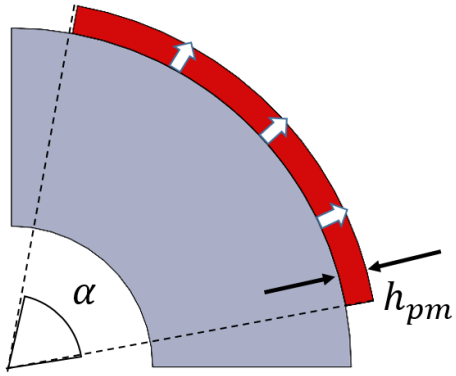

Fig. 4. One pole pitch of the SPM rotor. The magnetization direction is shown by white arrows

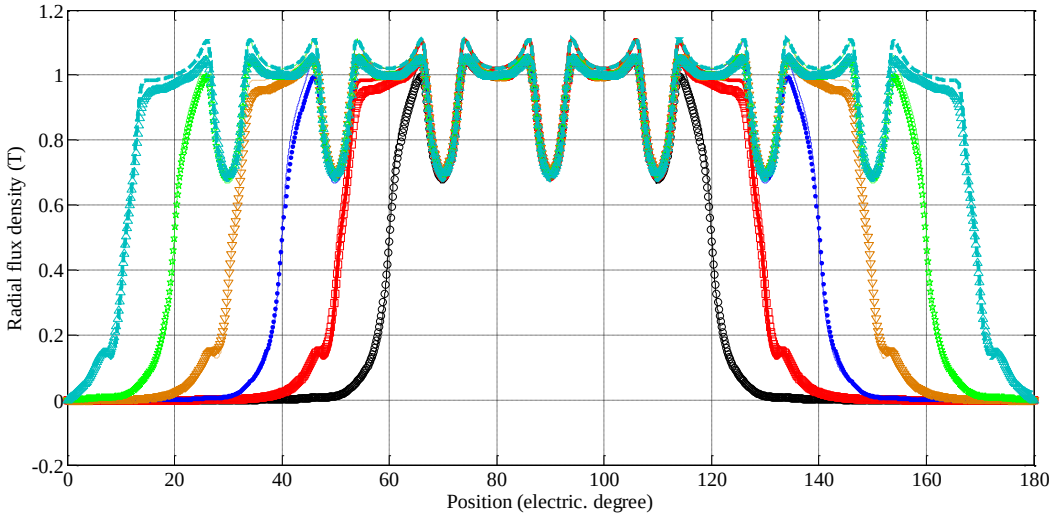

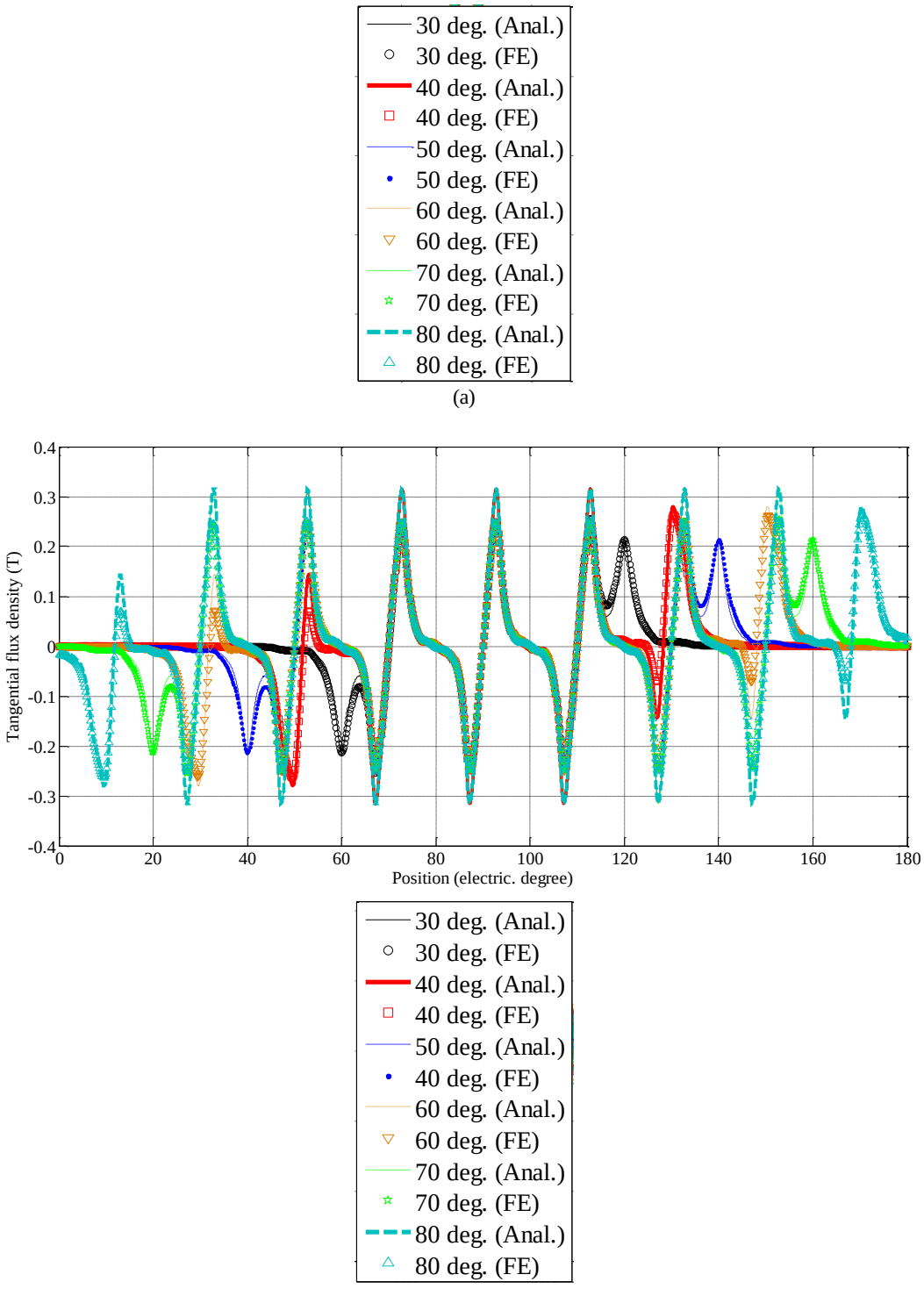

Fig. 5. Computed PM flux density in the air-gap for one pole pitch, analytical vs. FE results: (a) radial, and (b) tangential components

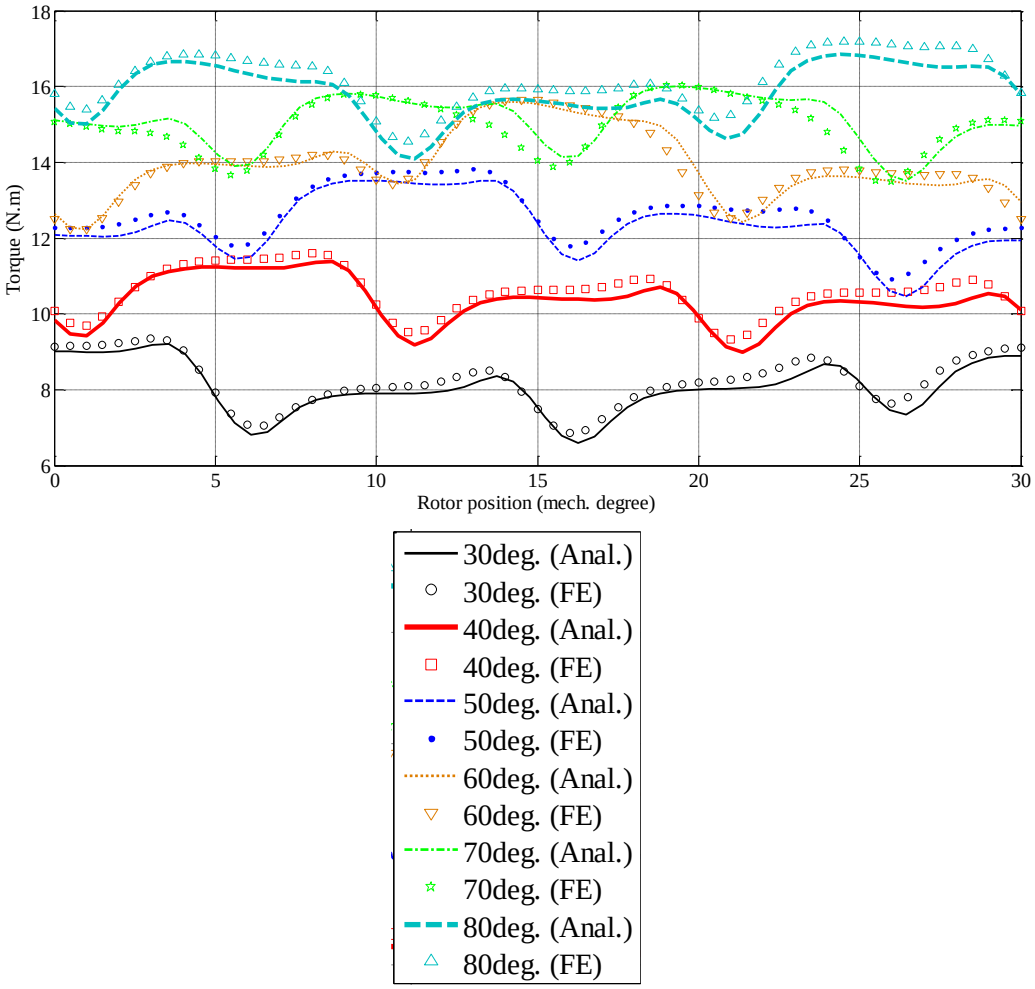

Fig. 6. Computed torque profile for various PM arc angles, analytical vs. FE

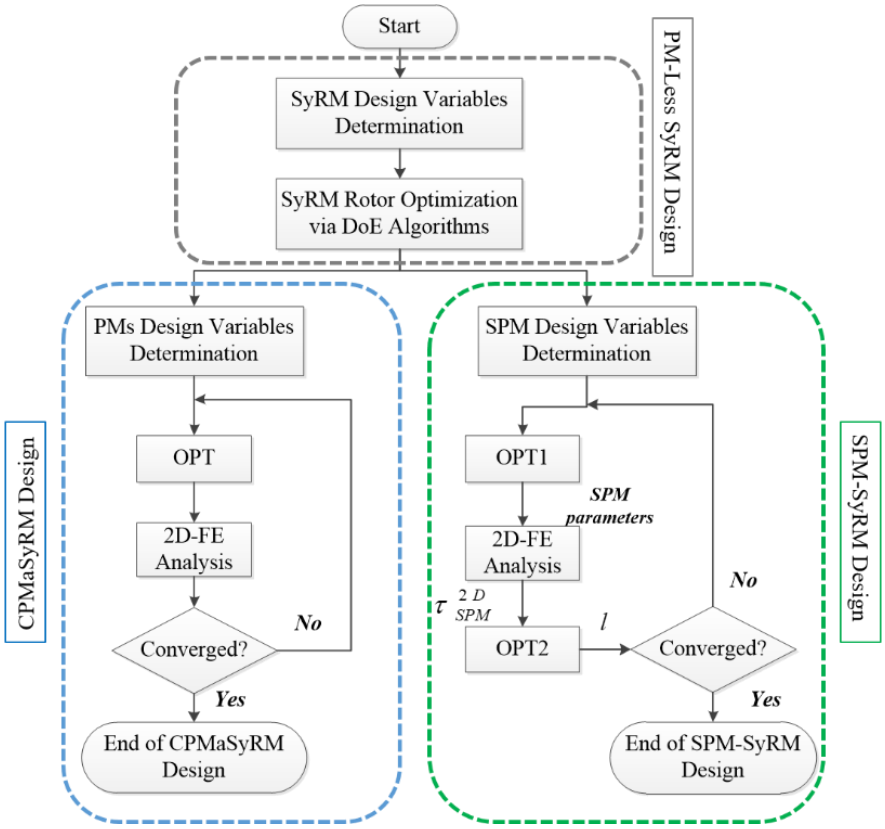

Fig. 7. The implemented design procedure towards CPMaSyRM and SPM-SyRM optimization

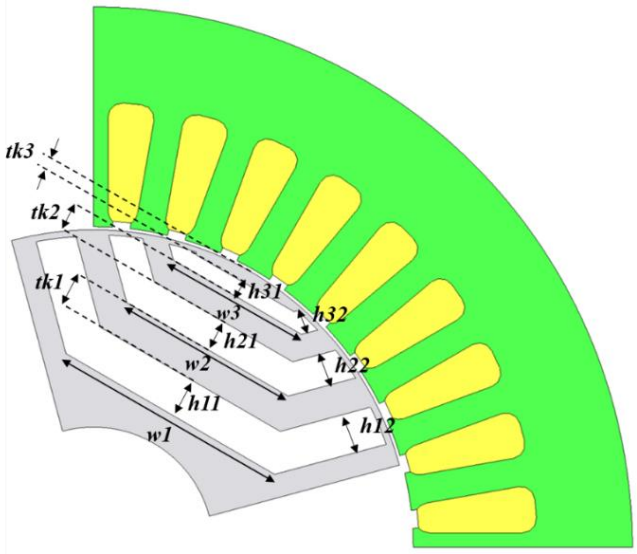

Fig. 8. One pole pitch view of the studied SyRM along with the rotor design parameters

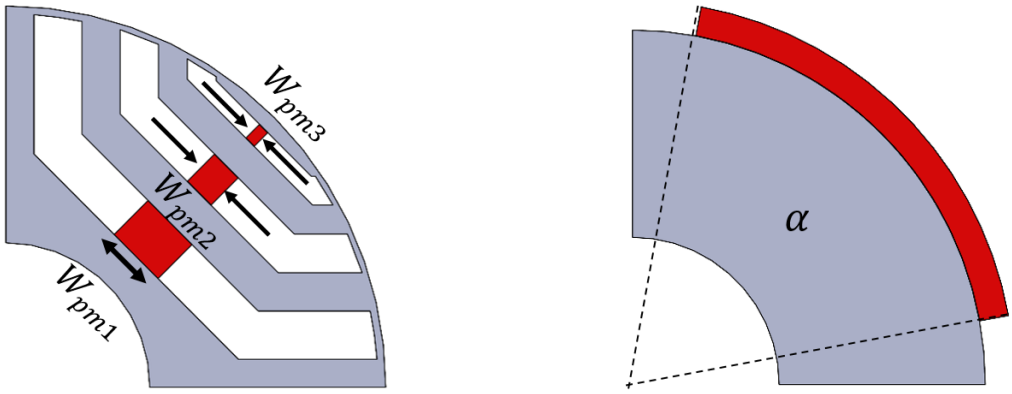

Fig. 9. The PMs design parameters of (a) CPMaSyRM, and (b) SPM segment of SPM-SyRM

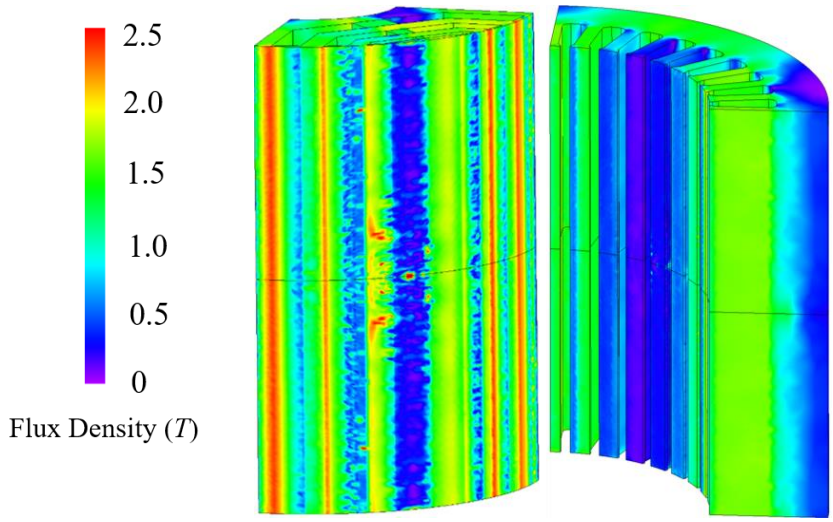

Fig. 10. 3D FE analysis of the optimized CPMaSyRM: loaded flux density contour

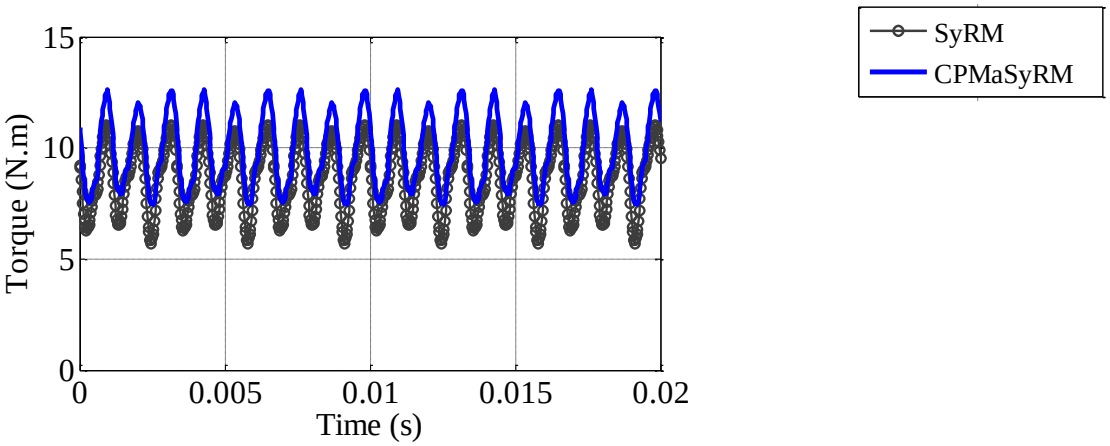

Fig. 11. Full load torque profile comparison of SyRM and CPMaSyRM

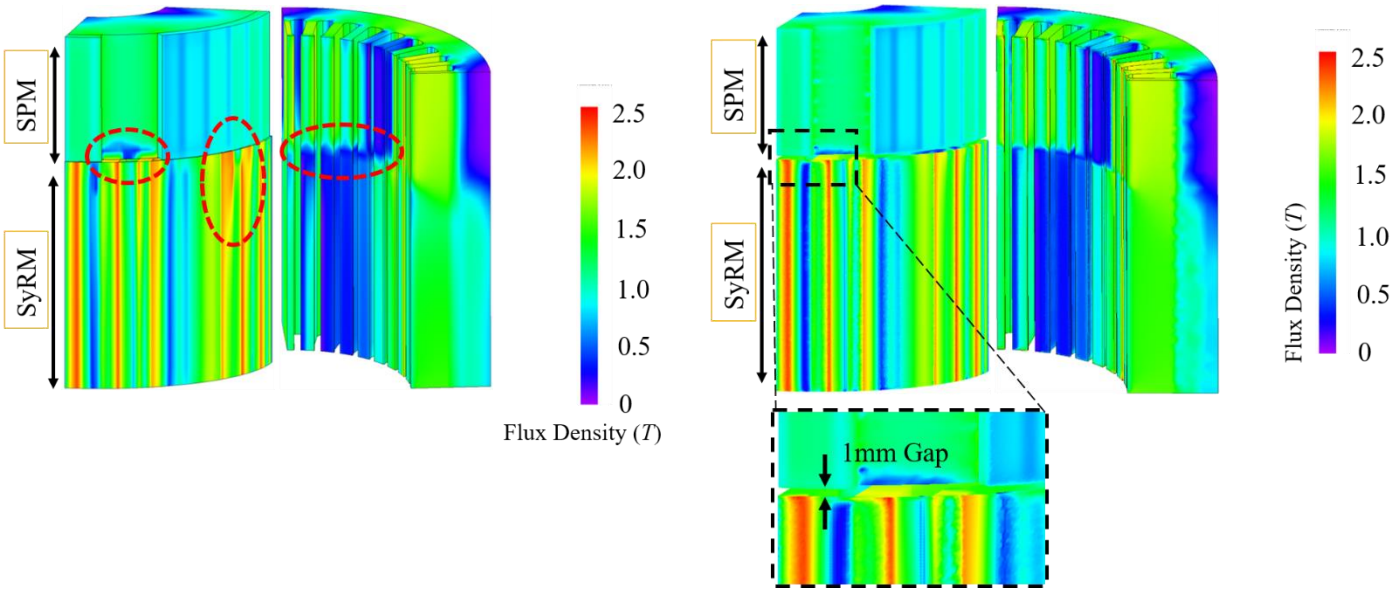

Fig. 12. 3D FE analysis of the optimized SPM-SyRM: loaded flux density contour without axial gap (left), and with axial gap (right)

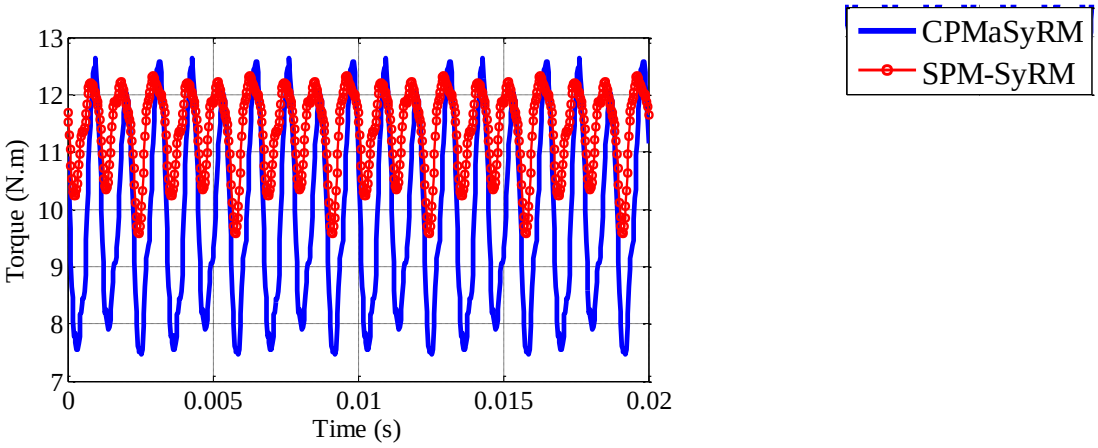

Fig. 13. Full load torque profile comparison of CPMaSyRM and SPM-SyRM

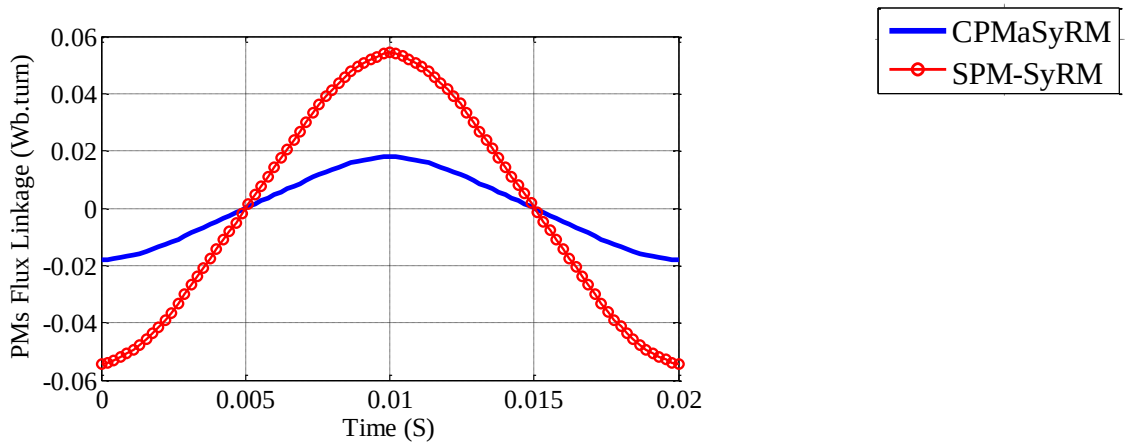

Fig. 14. PMs flux linkage comparison of CPMaSyRM and SPM-SyRM

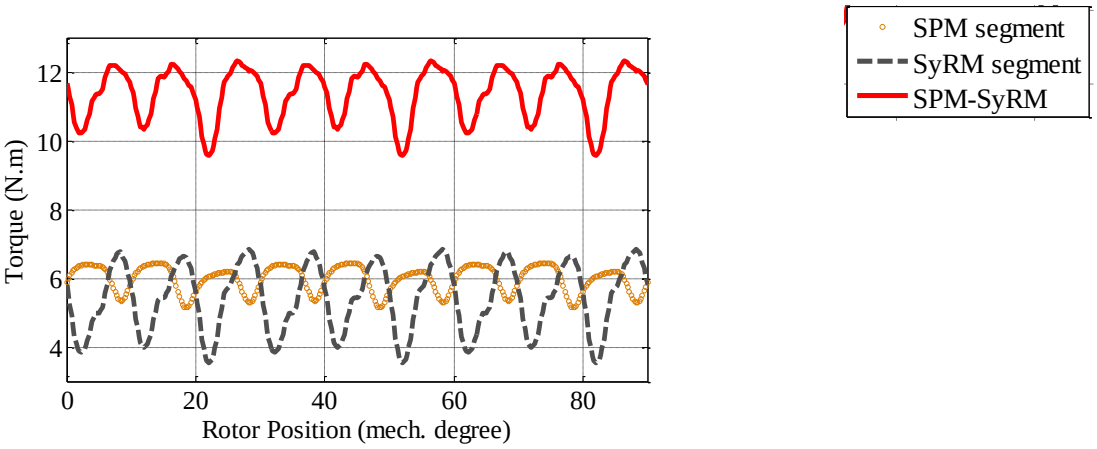

Fig. 15. Illustration of the SPM-SyRM total ripple reduction

TABLE I
Studied Motor Rated Specifications

Parameter	Value
Rated power	1.5 kW
Rated speed	1500 RPM
Rated frequency (*f*)	50 Hz
Rated phase current	38.7 Amax

TABLE II
Main Dimensions and Stator parameters

Parameter	Value
Pole number	4
Stator slot numbers	36
Stator outer diameter	135 mm
Rotor outer diameter	80 mm
Air-gap	0.4 mm
Stack length	100 mm
Slot fill factor	40%
Stator yoke height	12 mm
Winding factor	96%

TABLE III
The calculated SyRM with maximized reluctance torque

SyRM Rotor Parameters	Value (in [mm])
$[w_1, h_{11}, h_{12}, tk_1]$	$[26, 5, 5, 4.3]$
$[w_2, h_{21}, h_{22}, tk_2]$	$[20, 4, 4, 3.5]$
$[w_3, h_{31}, h_{32}, tk_3]$	$[14, 2, 3, 1.6]$
Torque characteristics @ rated current	**Value**
Mean torque	8.71 N.m
Ripple rate	61 %

TABLE IV
The optimized parameters of CPMaSyRM and SPM-SyRM

Motor	Parameter	Value
CPMaSyRM	W_{pm1}	6.5 mm
	W_{pm2}	3.5 mm
	W_{pm3}	1.25 mm
SPM-SyRM	α	69.3 deg.
	l	0.645

TABLE V
Torque characteristics and PM usage of the optimized designs SyRM, CPMaSyRM and SPM-SyRM

Motor	Characteristic	2D FE	3D FE
SyRM	Mean torque	8.9 N.m	8.71 N.m
	Ripple rate	59%	61%
	PM volume	0.0 cm3	
	PM flux linkage	0.0 Wb.turn	
CPMaSyRM	Mean torque	9.99 N.m	9.9 N.m
	Ripple rate	47.4%	52.4%
	PM volume	19.6 cm3	
	PM flux linkage	0.017 Wb.turn	
SPM-SyRM	Mean torque	11.69 N.m	11.37 N.m
	Ripple rate	22.6%	24.2%
	PM volume	19.6 cm3	
	PM flux linkage	0.0518 Wb.turn	

TABLE VI
Loss, efficiency, and power factor of the optimized designs

Characteristic	SyRM	CPMaSyRM	SPM-SyRM
Power Factor (%)	66.5	76.3	83.5
Efficiency (%)	87.8	89.2	90.3
Copper loss (W)	139.3	139.3	139.3
Iron loss (W)	50.9	49.5	52.5